Characterization of near-wall structures in the log-region of a turbulent boundary layer by means of conditional statistics of tomographic PIV data

Fabio J.W.A. Martins, Jean-Marc Foucaut, Michel Stanislas, Luis Fernando A. Azevedo

Characterization of Near-Wall Structures in the Log-region of a Turbulent Boundary Layer by Means of Conditional Statistics of Tomographic PIV Data

Fabio J. W. A. Martins[1,2], Jean-Marc Foucaut[2,3], Michel Stanislas[3] and Luis Fernando A. Azevedo[1]

[1]Mechanical Engineering Department, PUC-Rio, Brazil
[2]Univ. Lille, FRE 3723 LML Laboratoire de Mécanique de Lille, F-59000 Lille, France
[3]Centrale Lille, F-59000 Lille, France

Abstract

The random-in-appearance turbulent flow of boundary layers seem to display packages of organized coherent structures near the wall. The understanding of the generation and interaction of these structures and their contribution to the production and dissipation of turbulence is of great relevance to the modelling and control of wall-bounded flows. The present work is a contribution to the knowledge about organized coherent structures at the logarithmic region of turbulent boundary layers at relatively high Reynolds number. From a six-camera tomo-PIV experiment, conducted in a wind tunnel with a Reynolds number based on the momentum thickness of 8500, conditional statistics were obtained that allowed the characterization of low- and high-speed regions, ejections, sweeps and vortices. The analyses confirmed findings from previous works in the literature regarding ejection and sweep structures as being major contributors to the turbulent production, while vortices are responsible for dissipating this energy in the self-sustaining turbulent process. The vortical structures were found to be close to low-speed regions, being responsible to maintain these regions and to induce ejection and sweep events. The conditional statistics on the coherent structures at the log-region obtained in the present work were in good agreement with the literature, including statistics at the inner and outer regions of the canonical flow of a flat plate boundary layer, which suggest some possible general structure organization.

1 Introduction

The study of organized structures in turbulent boundary layers is of great relevance to the understanding, modelling and control of wall-bounded flows. For more than 60 years researchers attempt to understand the generation and interaction of these structures and their contribution to the production and dissipation of turbulence.

Coherent structures, which may also be referred as turbulent structures, are classified as organized motions that are persistent in time and space and are related to the transport of mass, momentum and heat. The first proposition for the organization of coherent structures in wall-bounded flows was due to Theodorsen (1952). In his model, the instability of the streamwise instantaneous velocity profiles would be responsible to create spanwise vortices due to a Kelvin-Helmholtz instability mechanism. These vortices under the action of the mean velocity gradient and instabilities of the flow, would be stretched, intensified and lifted away from the wall to regions of higher velocity, where further stretching would occur. The so deformed vortex tubes would evolve into streamwise or hairpin vortices. These vortical structures would be after associated with the formation of the low-speed streaks (Kline et al., 1967) close to the wall and with the mass transfer away from the wall, characterizing the ejections and bursting process in the buffer layer (Corino and Brodkey, 1969). The bursts, associated to the passage of intense vortices, reach the outer part of the boundary layer. This outward mass transfer is compensated by

sweep motions toward the wall. The combined action of these events occurring close to the wall produces turbulence at that region, that would be later transported and diffused by the turbulent bulges. The general shape of these vortex tubes could be visualized from the experimental studies made by Head and Bandyopadhyay (1981) that detected vortical structures in the form of arches, horse shoes and hairpins with legs preferentially inclined at 45° with the wall.

Smith and Walker (1997) proposed a model for the interaction among the multi-scale coherent structures present in the inner and outer layers of a boundary layer that rationalized the continuously self-sustaining turbulent process and the near-wall structure organization. According to this work, hairpin vortices in a shear flow are able to interact with other three-dimensional vortices to yield larger-scale flow structures, and regenerate new vortices through an interaction with the viscous wall layer (viscous-inviscid interactions). More recently, Lozano-Durán and Jiménez (2014) described merging and branching effects of vortices due to self-similar inertial processes, as well as splitting fragments of structures that lead to a wide range of scales.

Direct Numerical Simulation (DNS) has provided detailed insights into the near-wall structures in turbulent flows at low and moderate Reynolds numbers (e.g., Zhou et al., 1999, Schoppa and Hussain, 2002, del Álamo et al., 2006, Kang et al., 2007, to mention just a few). Specially, the study of Robinson (1991) found that, other than complete hairpin vortices, the wall layer was more populated with asymmetric cane-shaped vortices, which play an important role in the structure organization. Besides delivering computed fields well-resolved in space and time, DNS technique is able to manipulate the flow momentum equations in different ways, in order to validate conceptual models (Jiménez, 2013). Boosted by the development of computer power, DNS solutions are now able to reach elevated Reynolds numbers that allow the development of a reasonable log region in channel and boundary layer flows.

Particle Image velocimetry (PIV) also has made a significant contribution to the understanding of the flow organization near the wall in recent years. Adrian et al. (2000) performed PIV measurements in a streamwise-spanwise plane in a zero-pressure gradient boundary layer. They proposed a model of hairpin packets that travel along with low-speed region and populate the log-layer. Each package is formed by a train of aligned hairpins, which grow upwards in a ramplike arrangement inclined at a characteristic angle near 12°, that maintain the low-momentum regions between their legs. Several other researchers employed different PIV implementations, searching for insights into the organization of the boundary layer structure (e.g., Christensen and Adrian, 2001, Wu and Christensen, 2006, Stanislas et al., 2008, Dennis and Nickels, 2011a, Herpin et al., 2013). In particular, the two-plane stereoscopic PIV work of Ganapathisubramani et al. (2006) provided information on the full velocity gradient tensor that was employed to determine vortex core locations, orientation and sizes. Lin (2006) employed stereoscopic measurements in several planes parallel to the wall in the buffer layer of a flat plate boundary layer together with scalar functions to define appropriately flow structures as low- and high-speed regions, ejection sweeps and vortices. Recently, Stanislas (2017) presented a summary of advances in optical techniques that contributed to the understanding of the structure of the near and outer wall regions of boundary layer flows at elevated Reynolds number. At these high Reynolds number values, an outer turbulence peak was revealed.

Despite the increasing knowledge on near-wall turbulence accumulated by experiments and computation, some aspects related to which would be the type of relevant coherent structures that compose an organised model and which would be the model that could explain all aspects observed in turbulent flows remain not a consensus (Jiménez, 2013, Lozano-Durán and Jiménez, 2014). For instance, del Álamo et al. (2006) presented a different approach from that of Adrian et al. (2000) based on the analyses of direct numerical simulations and experiments in channel and boundary layer flows. They proposed a wake model, where clusters composed by disorganized vortices with different shapes are parts of larger structures of the streamwise velocity fluctuations whose average geometry resembles a cone. These vortex clusters are classified into two groups, self-similar wall-attached and detached ones. For high Reynolds number boundary layers, organized structures, with inner scaling, very near the wall seem to interact with very-large scale motions (Balakumar and Adrian, 2007), with outer scaling, in the outer region in a complex non-linear and unsteady coupling mechanism (Jiménez, 2013). In this context, the vortex

cluster model of del Álamo et al. (2006) seems capable of explaining the outer region, which approaches isotropic turbulence (Stanislas et al., 2008), while the model of cane vortices straddling low-speed structures proposed by Schoppa and Hussain (2002) seems more adequate to describe the inner region. The full description of near-wall organization models, as well as the mechanisms of generation and interaction of these coherent structures are beyond the scope of the present paper.

Recently, the development of Tomographic PIV (tomo-PIV) gave access to time-resolved full three-dimensional information on the flow field (Elsinga et al., 2006, Scarano, 2013). Despite the fact that the spatial resolution of current tomo-PIV implementations are lower than those of well-resolved stereo-PIV experiments, valuable information can be acquired from its full three dimensional capability (Scarano, 2013, Schröder et al., 2011). As pointed out by Gao et al. (2011), although in the boundary layer the dominant mean velocity gradient is dU/dy (y being the wall-normal coordinate and U the mean streamwise velocity component), the mean absolute value of all nine components of the velocity gradient tensor are of the same order, for a wall-normal coordinate of approximately 100 wall units. So, the availability of the full velocity gradient tensor yields more reliable estimates of relevant quantities such as vorticity, dissipation, and vortex detection criteria that are based on velocity gradient information.

Until now, just a few investigations have employed the tomo-PIV technique seeking the study of the near-wall organization in turbulent boundary layer flows (e.g., Elsinga et al., 2010, 2012, Jodai and Elsinga, 2016). Besides, most tomo-PIV experiments performed delivered only instantaneous visualizations about coherent organization, since they obtained insufficient amount of uncorrelated velocity fields in order to be able to provide reliable statistical results on turbulent structures.

The objective of the present work was to contribute to the understanding of the organization of the logarithmic region of turbulent boundary layers at relatively high Reynolds number. The focus of the work was directed to provide conditional statistical results to characterize low- and high-speed regions, ejections, sweeps and vortices obtained from a six-camera, tomo-PIV experiment conducted in a flat plate boundary layer flow in a wind tunnel with a Reynolds number Re_θ of 8500.

2 Experimental Setup

The turbulent boundary-layer experiment was carried out in the Laboratoire de Méchanique de Lille by the end of 2010 (Foucaut et al., 2011). The wind tunnel of this laboratory facility can produce boundary layers thicknesses of about 300 mm for a Reynolds number based on the momentum thickness of 8500. More details of this 1-m high, 2-m wide, 20-m long wind tunnel can be found in Carlier and Stanislas (2005). The experiment was operated with a free streamwise velocity of 3.6 m/s$\pm$0.5% with air at a temperature of 15$\pm$0.2°C in a close-loop configuration.

It is important to mention that the wind tunnel employed has a constant cross section, which imposes a slight constant pressure gradient on the boundary layer (Carlier and Stanislas, 2005). Nevertheless, the physics close to the wall of the present flat plate boundary layer flow are common to those of the zero pressure gradient boundary layer flow, and also to those of the channel flow (Carlier and Stanislas, 2005, Stanislas et al., 2008, Stanislas, 2017).

Poly-ethylene glycol smoke, which produces 1-μm particles, was employed to seed the flow. The particle image concentration was maintained at about 0.05 particles per pixel (ppp), equivalent to a source density N_s of about 0.16, for all the experiments conducted and reported in the present work.

The tomographic PIV setup was composed of 6 high-speed cameras (4 Phantom and 2 Photron) recording a spanwise-wall-normal volume produced by a Quantronix laser (2x30 mJ @ 1kHz) according to Figure 1. The cameras were mounted on Scheimpflug adaptors positioned under the wind tunnel in a forward scattering circular configuration. The Phantom V9.0 cameras (1600x1200 pixels @ 1000 fps) and Phantom V10 camera (2400x1800 pixels @ 480 fps) were set with micro Nikkor 200-mm lenses at f# 5.6, while the Photron Fastcam APX cameras (1024x1024 pixels @ 2000 fps) were set with micro Nikkor 105-mm lens at f# 5.6 equipped with a doubler. This tomographic arrangement led to a digital imaging resolution of about 17 pixel/mm, and particle-image diameters of about 1-2 pixels. The laser light sheet, coming from the top of the wind tunnel, produced a thin volume normal to the flow direction x. Its

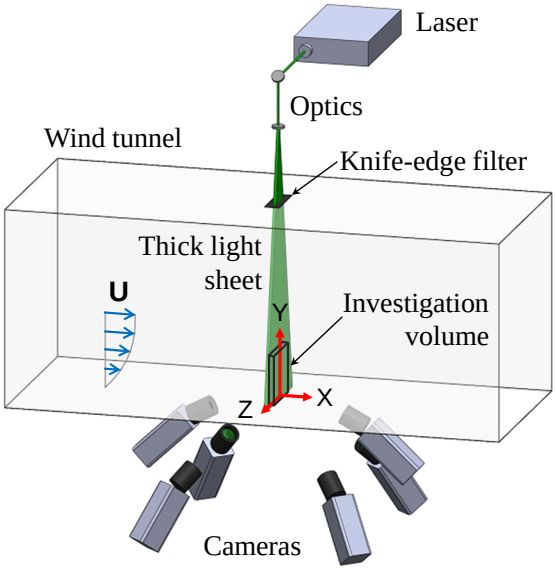

Figure 1: Sketch of the cameras arrangement in the boundary layer experimental setup.

thickness was limited to 5 mm by a knife-edge filter to create an investigation volume of 5x45x45 mm^3 (i.e., 50x450x450 wall units).

3 Tomo-PIV Processing

The cameras were calibrated by a pinhole model from 7 equally-spaced calibration planes followed by a self-calibration procedure (Wieneke, 2008). The final camera mapping functions had projection errors of about 0.01 pixel and maximum triangulation errors lower than 0.18 pixel (Martins et al., 2015b).

A parallelized tomo-PIV software (Thomas et al., 2014) was employed to process the acquired particle images. The particle images were pre-processed by a minimum-history background subtraction operation, followed by a 3x3-pixels Gaussian-filter smoothing (Martins et al., 2015b). The pre-processed images were reconstructed by means of 8 iterations of BIMART algorithm with MinLOS initialization (Thomas et al., 2014). A 2-iteration volume-filter threshold of 0.003 was adopted to reduce the amount of ghost particles. The 3D reconstructed volume was produced employing a pixel to voxel ratio of 0.8 and a volume enlargement along the thickness of 15% in order to increase the quality. The final volumes were composed by 74x644x644 cubic voxels with side dimensions of 0.07 mm. The quality of the reconstructed volumes was accessed during a thorough tomo-PIV optimization study and were within the suggested values from the literature (Martins et al., 2015b).

A total of 8620 velocity fields were computed from pairs of volumes containing the reconstructed particle distributions by means of a 3D multi-pass cross-correlation with sub-pixel shift. The final interrogation volume had the size of 36x36x36 pixels (i.e., 26x26x26 wall units) with 75% of overlap, leading to a final field grid of 5x67x67 vectors. The amount of reconstructed particles inside the final interrogation volumes was between 5 to 10, checked by visual inspection. The time delay employed of 300 μs led to an average particle displacement of about 10 voxels. The spurious vectors, classified by a normalized median filtering (Thomas et al., 2014), of about 1.5% were successfully replaced by the interpolation of their adjacent neighbours. Figure 2 presents three orthogonal slices of a typical instantaneous velocity field coloured by magnitude of the streamwise velocity component. In the middle plane, one over each three velocity vectors are presented, representing the wall-normal and spanwise velocity components.

More details on the experimental setup of the present work, the data base acquired and the tomo-PIV processing can be found in Foucaut et al. (2011) and Martins et al. (2015b).

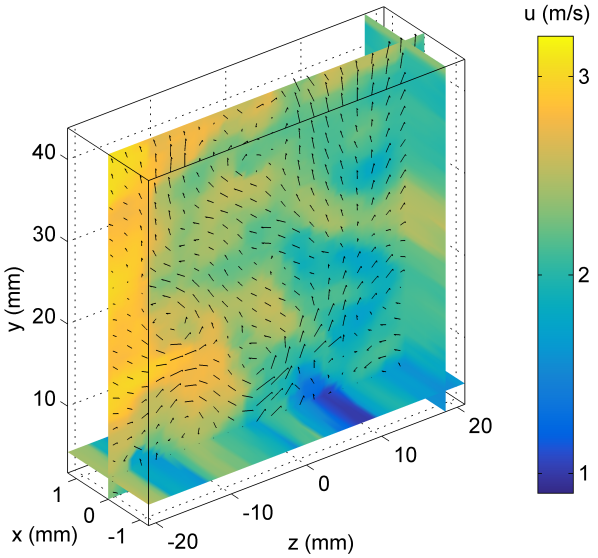

Figure 2: Sample of three-dimensional three-component instantaneous velocity field. One over each three velocity vectors are plotted for clarity.

4 Uncertainty Analyses

The reported uncertainty levels associated with the measurements of the present study refer only to the type B uncertainties, also termed in the literature as systematic uncertainty, which is related to the measurement method, other than the statistical analysis of series of observations (BIPM et al., 2008). The type A uncertainty component, also referred as random uncertainty component, was not evaluated here, since its influence on the total combined measurement uncertainty decreases with the amount of statistically independent samples considered (BIPM et al., 2008).

The uncertainty levels associated with the velocity measurements were estimated based on the root-mean-square of the divergence of the instantaneous velocity field $({}^{\partial u_i}/_{\partial x_i})_{rms}$, according to Atkinson et al. (2011). The velocity gradients along the x, y and z directions were computed by a second-order central difference scheme from the 3C-3D velocity fields. Because, the divergence of the velocity field must be zero for an incompressible flow free of measurement errors, the magnitude of the computed divergence can be associated to the uncertainty levels. Assuming that the vector spacing $\triangle_{\text{vec}}$ and the local uncertainty in each direction are uniform, the uncertainty in the velocity components, $\delta(u)$, can be given as

$$\delta(u) \;=\; \sqrt{\frac{2\,{\triangle_{\text{vec}}}^2}{3}}\left(\frac{\partial u_i}{\partial x_i}\right)_{\text{rms}} \quad . \tag{1}$$

The root-mean-square of the velocity divergence, computed within the entire volume, was 67 s^{-1}, leading to a mean standard uncertainty in the velocity of the order of 0.15 voxel (equivalent to 0.035 m/s or 0.23 u_τ). The standard uncertainty, commonly reported in the literature by the name of uncertainty, is associated to a 1-sigma confidence level, which means that the true velocity value is expected to lie within the uncertainty interval of $\pm\delta(u)$ with a probability of 68%. The mean value of uncertainty computed was about 10% of the maximum u'_{rms} and 1% of the free stream velocity. The value of the standard uncertainty ranges from 0.30 voxel, very close to the wall, to 0.10 voxel, for high wall-normal positions. The higher uncertainty levels near the wall seem to be caused by the higher velocity gradients and lower velocities present at that region. In addition, the particle images closer to the wall suffered from light reflections from the wall, which increased the noise in the velocity fields.

The present uncertainty results were considered as a low level of uncertainty for a tomo-PIV air experiment, and were probably achieved due to the measurements performed in a narrow volume employing 6 cameras. This uncertainty level was comparable to well-controlled tomo-PIV experiments found in the

literature (e.g., Atkinson et al., 2011, Fuchs et al., 2016).

The uncertainties in each velocity derivative computed by the central-difference scheme can be estimated by uncertainty propagation, following the guide to the expression of uncertainty in measurement of BIPM et al. (2008). The standard uncertainty in the velocity derivatives, considering negligible uncertainties in the vector spacing compared to the uncertainties in the velocity components and ignoring cross-correlation terms, simplifies to

$$\delta\left(\frac{\partial u_i}{\partial x_j}\right) \;=\; \frac{\sqrt{2}}{2\,\triangle_{\mathrm{vec}}}\,\delta(u_i) \quad . \tag{2}$$

It is well know that velocity derivatives increase the noise level already presented in the velocity. Also, eq. 2 gives a slight overestimation of the uncertainty in the velocity derivatives, since it does not take into account the correlation between the uncertainties of velocity vector components due to the overlapped interrogation volumes employed for performing the velocity computation (Sciacchitano and Wieneke, 2016). In the present study, this conservative estimation is used in order to give an upper bound for the computed uncertainty levels, yielding a measure of the capability of our measurements in delivering quantitative information related to quantities obtained from derivatives of the flow field.

The uncertainty levels in each component of the vorticity vector were computed using the uncertainties in the velocity derivatives. Assuming negligible uncertainties in the vector spacing, no cross-correlation terms and similar local uncertainties in the velocity components, the standard uncertainties in the vorticity components can be simplified as

$$\delta(\omega_k) \;=\; \frac{\sqrt{2\left(\delta(u_i)^2+\delta(u_j)^2\right)}}{2\,\triangle_{\mathrm{vec}}} \;=\; \frac{\delta(u)}{\triangle_{\mathrm{vec}}} \quad . \tag{3}$$

The mean value of the standard uncertainty in the instantaneous vorticity components was about 55 s^{-1} (equivalent to 0.017 voxel/voxel or $0.036\,u_\tau^2/\nu$ in wall units). As the uncertainty in the vorticity is related to the uncertainty in the velocity, the highest standard uncertainty value of the instantaneous vorticity, equal to 0.034 voxel/voxel, was observed near the wall. The levels of uncertainty found in the present work are similar to the vorticity uncertainty levels reported by Sciacchitano and Wieneke (2016) for PIV measurements of a turbulent flow experiment in a cavity.

Since tomo-PIV gives access to the full velocity gradient tensor, as already mentioned, the rate of dissipation of turbulence kinetic energy by viscous stresses, for a Newtonian incompressible fluid, can be calculated according to Foucaut et al. (2016).

$$\epsilon \;\equiv\; 2\,\nu\,S_{ij}^2 \tag{4}$$

where $S_{ij} = (1/2)(\partial u_i/\partial x_j + \partial u_j/\partial x_i)$.

The standard uncertainty in the dissipation rate can be computed from the combination of the uncertainties, assuming equivalent uncertainties of spatial derivatives along all directions, negligible uncertainties in the vector spacing and in the kinematic viscosity, and no cross-correlation terms.

$$\delta(\epsilon) \;=\; \sqrt{8\,\nu\,\epsilon}\;\delta\left(\frac{\partial u_i}{\partial x_j}\right) \tag{5}$$

The mean value of the standard uncertainty in the rate of dissipation obtained was about 0.30 m^2/s^3, which is equivalent to $0.009\,u_\tau^4/\nu$ in wall units.

Besides the uncertainty, it is important to discuss about spatial filtering effects and noise in the computation of the flow quantities, in special the dissipation. The interrogation volume size used to compute the velocity field in the tomo-PIV experiments corresponded to IV=26x26x26 wall units, which was equivalent to approximately $8\,\eta_k$ (Kolmogorov length scale) in each direction (considering $\eta_k \approx$ 3 wall units from Carlier and Stanislas, 2005). Given that the diameters of the most intense vortical structures were reported to be around 6 to $10\,\eta_k$ (Stanislas et al., 2008, Herpin et al., 2013, Lozano-Durán and Jiménez, 2014), it is conceivable that those small vortices were filtered out by the correlation

Table 1: Boundary-layer characteristics.

U_∞ (m/s)	ν (m^2/s)	θ (m)	δ (m)	u_τ (m/s)	δ_ν (m)	Re_θ	Re_δ
3.6	1.50x10^{-5}	0.0354	0.300	0.147	1.00x10^{-4}	8500	72000

procedure. So, it is expected that the dissipation rate should be marginally underestimated. In addition, it is important to mention that the computation of dissipation rate from the tomo-PIV data carried a considerable level of uncertainty, mainly due to the multiplication of spatial derivatives that are known to add noise to the results.

5 Flow Statistics Results

Although a 1 kHz, time-resolved, tomo-PIV experiment was carried out, the statistics were calculated using 1204 time-independent velocity fields with a time separation of 0.01 s. This time interval was necessary to guarantee decorrelation of the captured flow fields (following Sciacchitano and Wieneke, 2016), since the focus of the study presented in this article was on flow and coherent structure statistics of the boundary layer and not on instantaneous turbulent structure visualizations.

Table 1 summarizes the boundary-layer properties of the present wind-tunnel experiment, such as free stream velocity (U_∞), kinematic viscosity (ν), momentum thickness (θ), boundary-layer thickness (δ), friction velocity (u_τ), viscous length scale (δ_ν) and Reynolds numbers based on the momentum thickness (Re_θ) and on the boundary-layer thickness (Re_δ). The friction velocity was estimated from a Clauser plot of the velocity profile inside the log region, analogous to that presented in Stanislas et al. (2008), using the von Kármán empirical constants κ=0.41 and C=5.

Figure 3(a) compares velocity statistics from the present tomographic PIV reconstruction with hot-wire anemometer data (HWA) obtained in the same wind tunnel for a boundary layer with $Re_\theta = 8170$ (Carlier and Stanislas, 2005). The direct numerical simulation (DNS) for a turbulent channel flow with Re_τ of 2000 of Hoyas and Jiménez (2008), the Van Driest profile and the log law are also presented for comparison. The plot is scaled by inner variables. From this figure, it can be verified that the tomo-PIV and HWA average velocity profiles are virtually identical and agree with the DNS, Van Driest and log-law profiles.

Good agreement between tomo-PIV and HWA data is also observed in figure 3(b) for the profiles of turbulent fluctuating velocity components. Deviations in the measurements from the two techniques are larger near the wall due to the presence of light reflections. It should be mentioned that the measurements of spanwise fluctuating velocity near the wall for the hot-wire are overestimated due to the size of the probe compared to the mean gradient at this region. For comparison, the direct numerical simulation of Hoyas and Jiménez (2008) with Re_τ of 2000 is also presented. The tomo-PIV experimental data overlap with DNS curves considering the estimated uncertainties. The agreement found in the measurements is an indication that the recording time was sufficient to obtain converged statistics.

Profiles of Reynolds shear stress, $- < u'v' > /u_\tau^2$, and main viscous stress, $(\partial U/\partial y)(\nu/u_\tau^2)$, obtained from the present tomographic PIV and hot-wire anemometer measurements from Carlier and Stanislas (2005), are presented in figure 4(a). Reynolds stress from the DNS study of Hoyas and Jiménez (2008) are also plotted for comparison. A remarkable agreement between the tomo-PIV measurements and the Van Driest profile can be verified in this figure. The DNS profile of Reynolds shear stress displays a slightly higher inclination for $y^+ > 50$ compared to the Van Driest profiles that might be attributed to small differences between channel and boundary layer flows at that region. The tomo-PIV measurements agree with the direct numeric simulation within the expected levels of uncertainty.

Figure 4(b) compares the mean dissipation rate, $\epsilon^+ = \epsilon(\nu/u_\tau^4)$, from tomo-PIV, computed according to equation 4, and that from HWA for the boundary-layer data with $Re_\theta = 8170$ of Stanislas et al. (2008), computed with the assumption of Taylor's hypothesis and small-scale isotropic turbulence. The dissipation rates from the direct numerical simulation of Hoyas and Jiménez (2008) are also plotted for comparison. As already mentioned, it was expected that the interrogation volume employed to compute

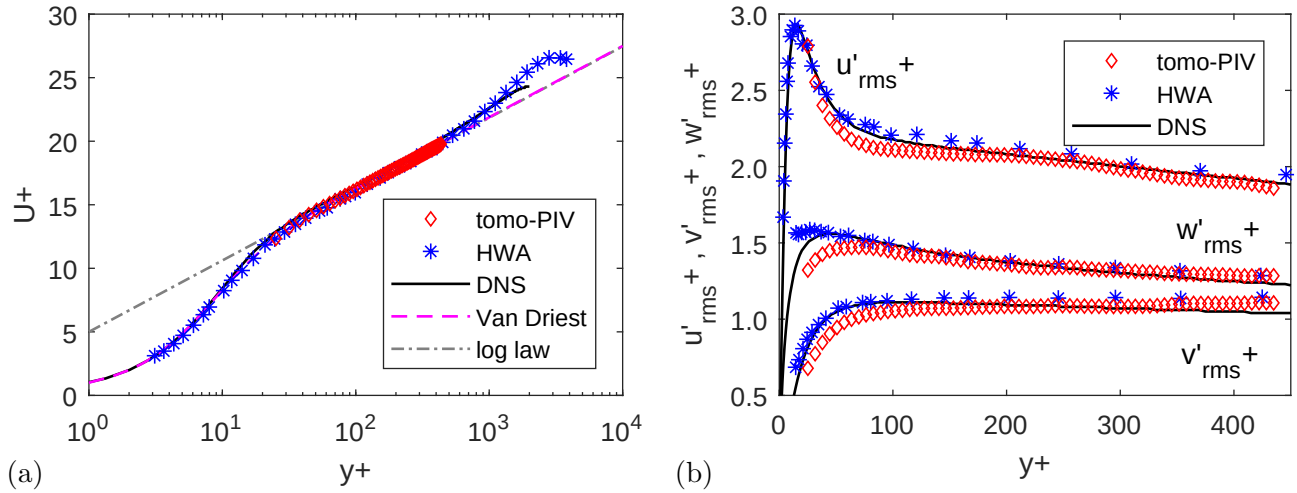

(a) (b)

Figure 3: Profiles of (a) mean streamwise velocity in semi-log plots and (b) turbulent velocity fluctuations made dimensionless by wall-units. Comparison with hot-wire anemometer measurements of Carlier and Stanislas (2005) and direct numerical simulations of Hoyas and Jiménez (2008).

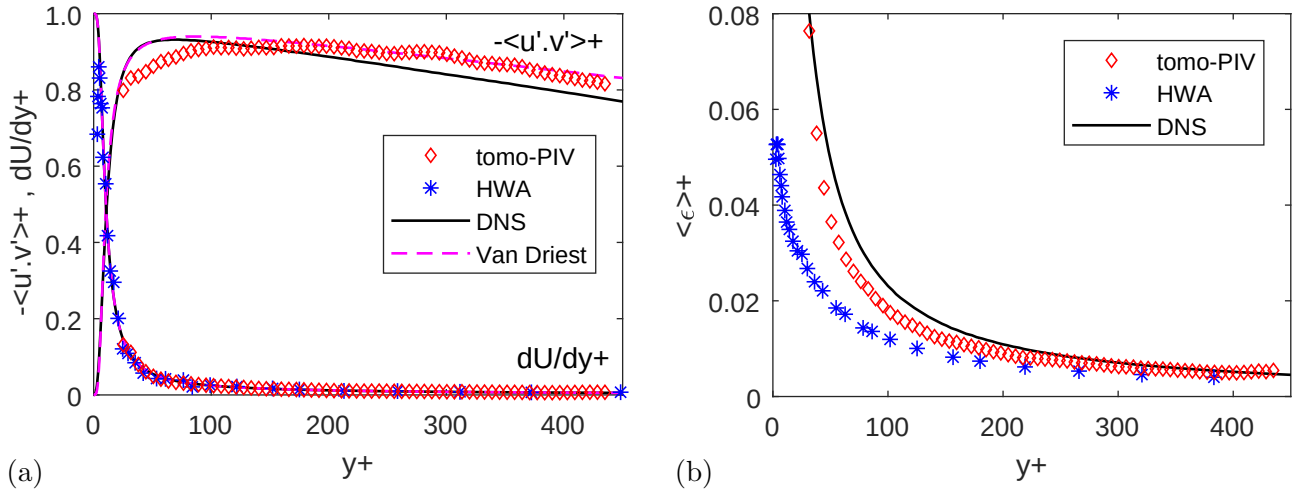

(a) (b)

Figure 4: Profiles of (a) Reynolds and viscous stress and (b) dissipation rate as a function of the distance to the wall. Comparison with hot-wire anemometer measurements (HWA) of Carlier and Stanislas (2005), Van Driest profile and DNS of Hoyas and Jiménez (2008).

the velocity field in the present work filtered the influence of smaller scales, and that the uncertainty of the computed dissipation rate would be high. Nevertheless, good agreement between the present tomo-PIV measurements and DNS data is observed. It is seen that the HWA measurements deviated from tomo-PIV and DNS results, for positions $y+ < 100$, where the size of the probe seems to be inadequate to resolve the smallest structures. Additionally, very close to the wall, the assumption of Taylor's hypothesis and local isotropic may fail. It should also be mentioned that the DNS Reynolds number is smaller than that of the wind tunnel flow, what yield smaller values for the dissipation rate. Higher dissipation rates are observed close to the wall, where the most stronger vortices in the near wall region were reported to be locate by the works available in the literature (Robinson, 1991, Stanislas et al., 2008).

All components of the vorticity vector can also be computed from the three-dimensional tomo-PIV measurements by means of a central-difference scheme. Figure 5 shows the root-mean-square of fluctuating vorticity components from the present tomo-PIV measurements and the DNS study of Hoyas and Jiménez (2008). The plot is scaled by inner variables. No filtering was employed. Although it is expected that tomo-PIV measurements underestimate the fluctuating vorticity components due to the interrogation volume size, both methods agree within the expected uncertainty levels.

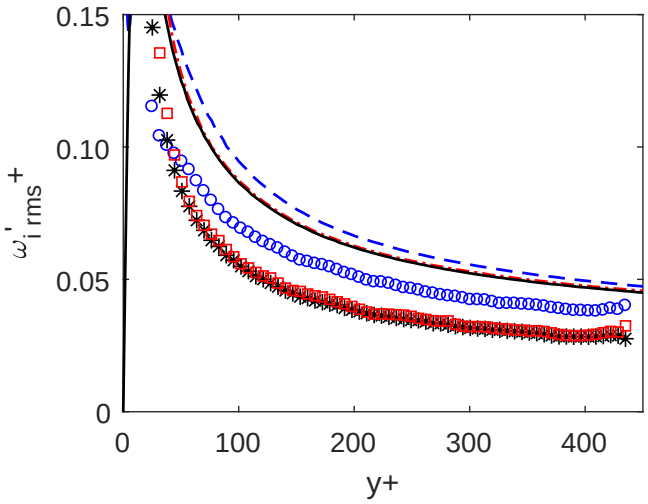

Figure 5: Comparison of profiles of root-mean-square of fluctuating vorticity components from tomo-PIV boundary-layer data and DNS of Hoyas and Jiménez (2008). Tomo-PIV profiles are displayed with markers, fluctuating stream-wise vorticity (∘), fluctuating wall-normal vorticity (∗) and fluctuating spanwise vorticity (□), while DNS profiles are displayed as lines, fluctuating stream-wise vorticity (– –), wall-normal vorticity (——) and spanwise vorticity (– · –).

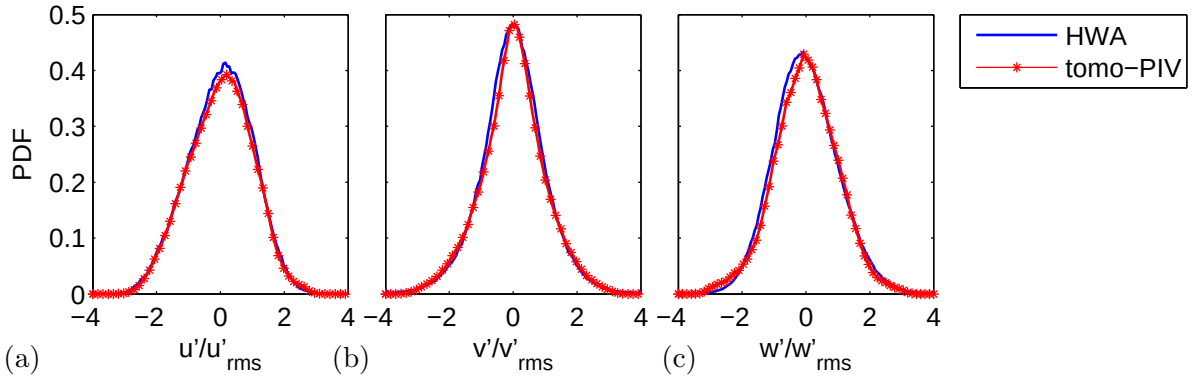

Figure 6: Probability density functions of the fluctuating velocity components at 50 wall units for (a) streamwise, (b) spanwise and (c) wall-normal directions of the present tomo-PIV measurements and the hot-wire quantification of Carlier and Stanislas (2005).

Figure 6 compares the probability densities function (PDF) of the three fluctuating velocity components calculated at 50 wall units by tomo-PIV and HWA. A general observation of the distributions for the three velocity components shows excellent agreement between tomo-PIV and HWA data, considering the prevailing levels of experimental uncertainty. Fig. 6(c) shows a marginal asymmetry in the tomo-PIV that, seemingly, was caused by a little reminiscence from the peak-locking effect, since the deformation method was not applied to the interrogation volume during the correlation process (Scarano, 2013), but only sub-pixel shift.

Figure 7 presents the power spectral density of the streamwise fluctuating velocity component of the present boundary-layer experiment at a wall-normal position of 100 wall units. The time-resolved velocity data records were divided into 512-size windows with 50% of overlap before computing the Fast Fourier Transform (FFT) in order to smooth the results. A specific treatment was employed on the FFT velocity windows to impose an artificial periodicity (Foucaut et al., 2004). In figure 7, the power spectral density is made dimensionless by the Kolmogorov length scale. The power spectral density of the hot-wire measurements for the same wind tunnel obtained by Carlier and Stanislas (2005) are also plotted for comparison. It is possible to observe a region displaying a slope close to -1 (related to energy-containing scale), another region of about -5/3 slope (related to the inertial range) and a stiffer slope region (related

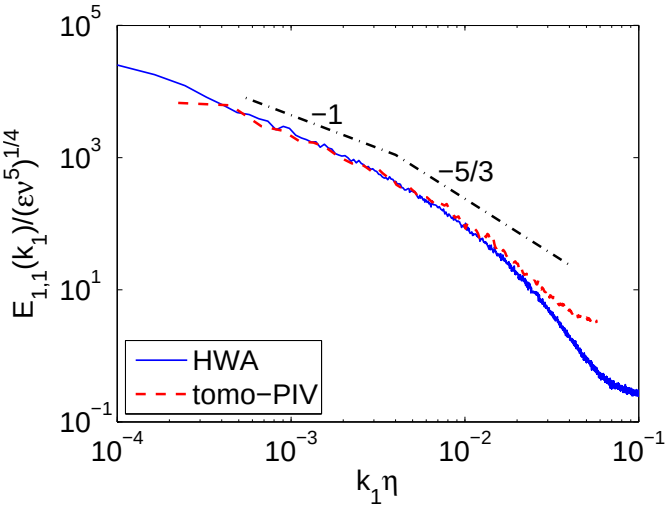

Figure 7: Power spectral density for the tomo-PIV streamwise fluctuation velocity component at 100 wall units as a function of the wavenumber dimensionless by the Kolmogorov length scale. The power spectral density for the hot-wire measurements of Carlier and Stanislas (2005) is plotted for comparison. Slopes are displayed as dash-dotted lines (−·−).

to dissipation). The inflection of the spectrum curve at high wavenumbers gives an idea of the noise and filtering levels associated with the tomo-PIV results. The tomo-PIV curve coincides with that of the HWA up to a certain wavenumber value. Although the tomo-PIV measurements of the present work have a cut-off wavenumber of $k_c\eta \approx 0.06$, given by the acquisition frequency, after the wavenumber value of $k_{max}\eta \approx 0.025$, the noise associated with these measurements exceeded that of the HWA. This is an expected result if one considers the size of the interrogation volume employed in the cross-correlation procedure (Foucaut et al., 2004, Atkinson et al., 2014).

6 Pattern Recognition of Turbulent Structures

The procedures employed to extract information on the coherent structure will now be described. The coherent structures studied in the present work were low- and high-speed regions, ejections, sweeps and vortices. The coherent structures were classified as continuous regions above or below empirical threshold values (F_{thresh}) selected for specific detection functions (F_d). Low- and high-speed regions were defined as locations of negative and positive fluctuating streamwise velocities, respectively, following previous works in the literature (Lin, 2006, Kang et al., 2007, Dennis and Nickels, 2011b, Dekou et al., 2016). Ejection and sweep events were detected by means of the quadrant-splitting scheme of the $u'v'$ signal (Wallace et al., 1972, Wallace, 2016). Quadrant Q2 ($u' < 0$ and $v' > 0$) is associated with ejections and quadrant Q4 ($u' > 0$ and $v' < 0$) with sweep events. Vortices were classified by employing the Q-criterion (Hunt et al., 1988, Chakraborty et al., 2005, Martins et al., 2016).

The Q-criterion identifies vortices as flow regions with positive second invariant of the velocity gradient tensor, i.e., $Q_{3D} > 0$. The Q-criterion for an incompressible flow is given according to Hunt et al. (1988) as

$$Q_{3D} = -\frac{1}{2}\frac{\partial u_i}{\partial x_j}\frac{\partial u_j}{\partial x_i} . \tag{6}$$

In the present study, all detection functions were normalized by their local root-mean-square value. Employing this metric, it is possible to generalise the detection function for different Reynolds number and to overcome variations in the detection function distribution along the wall-normal direction for wall-bounded turbulence. Indeed, in case a uniform high threshold value would be applied to a detection function with no normalization, proper detection of the vortices could be obtained at the near-wall region, while very few vortices would be detected at the outer region. Conversely, for lower threshold values,

Table 2: Coherent structure classification.

Coherent Structure	Detection Function	Flow Region	Threshold
Low-speed region	$F_d^{u'} = \frac{u'(x^+,y^+,z^+,t)}{u'_{\mathrm{rms}}(y^+)}$	$F_d^{u'} \leq F_{\mathrm{thresh}}^{u'}$	-1
High-speed region		$F_d^{u'} \geq F_{\mathrm{thresh}}^{u'}$	1
Ejection	$F_d^{u'v'} = \frac{u'v'(x^+,y^+,z^+,t)}{u'v'_{\mathrm{rms}}(y^+)}$	$F_d^{u'v'} \leq F_{\mathrm{thresh}}^{u'v'}$ and $F_d^{u'} < 0$	-1
Sweep		$F_d^{u'v'} \leq F_{\mathrm{thresh}}^{u'v'}$ and $F_d^{u'} > 0$	-1
Vortices	$F_d^{Q_{3D}} = \frac{Q_{3D}(x^+,y^+,z^+,t)}{Q_{3D\,\mathrm{rms}}(y^+)}$	$F_d^{Q_{3D}} \geq F_{\mathrm{thresh}}^{Q_{3D}}$	1

a correct detection of vortical structures at the outer layer would be attained while a confusing set of cluttered vortex tubes would be detected close to the wall.

The coherent structures where analysed only at the 2D middle planes (x^+=0) of the same 1204 time-independent velocity fields used to compute the flow statistics. Table 2 summarises the coherent structures classification employed. It is relevant to mention that, although the coherent structures were detected at the 2D mid-planes, all 3D information available from the tomo-PIV measurements were used in the detection of the structures. This is a distinct feature of the present work in relation to other studies where only 2D information on the flow quantities were available (e.g., Lin, 2006, Dekou et al., 2016).

The threshold values employed in the detection function fields influence the quantified statistical results within each coherent structure. The adequate threshold for each type of turbulent structure was selected in order to keep as many energetic structures as possible and, at the same time, to limit the noise level. The threshold values employed in the detection function fields were chosen after detailed preliminary tests based on the balance between the amount of detected turbulent structures, their shape, the energy content of these structures and the formation of regions comprehending spurious information. In the case of vortex regions, for instance, the use of a low threshold value created binary fields composed of small amount of large structures. By increasing the threshold value, the sizes of the structures were seen to decrease, leading to the disconnection of the structures. Over a certain value, around $F_{thresh}^{Q_{3D}} = 0.5$, the amount of vortices started to decrease. At that threshold level, the vortex structure seemed to be composed of an agglutination of vortices. Around $F_{thresh}^{Q_{3D}} = 1$ the general shape of the vortices seemed to be detected. For the other types of coherent structures, the inflection of the amount of structures with respect to the threshold level was not so evident. Over a certain range of threshold values, the general structure shape was not modified, and only slight changes were observed in their sizes and amount. However, increasing the threshold above a certain level decreased the influence of background noise. The increment of threshold value beyond the mentioned range, decreased the size and amount of detected structures. For all structures in the present work, threshold values equal to one standard deviation were adopted, which were in line with previous studies from our group (Carlier and Stanislas, 2005, Dekou et al., 2016). These adopted threshold values were sufficient to keep a representative amount of energy inside the coherent structures in relation to the surrounding flow (Dekou et al., 2016).

Classical morphological operations, as closing and opening (Gonzalez, 2009), were employed to remove small structures and fill empty spaces in the detected objects. The binary fields containing the coherent structures were filtered by one iteration of closing and opening operations, using a structuring, diamond-shape, 3x3 element. The watershed algorithm (Roerdink and Meijster, 2000) was adopted to split large turbulent regions into smaller connected regions in order to improve the convergence of statistical results. Then, a cleaning procedure was employed to remove structures with areas below 2 grids, which could be wrongly classified due to noise in the structure detection field.

Figure 8 exemplifies the classification of low- and high-speed regions, ejection and sweep events and vortices detected by the described procedure. The normalized detection function fields are displayed by the colourplots, while the detected turbulent structures are drawn as contours of different line colours

identified in the legend of the figure. A visual analysis of the results of figure 8, that are based on a single instantaneous velocity field, allows the observation of some interesting features. For instance, the ejections detected are not subregions of the low-speed regions due to the detection function and threshold level employed, although these two types of coherent structures are in close proximity. The same behaviour is observed regarding the sweeps and high-speed regions detected. It is seen that most of the vortices detected are found in the vicinity of low-speed regions and ejections. These observations, obtained by visual inspection of other instantaneous measured fields equivalent to the one displayed in figure 8, were expected from previous works found in the literature and will be discussed in the framework of the conditional statistics in the following section.

7 Conditional Statistics Results

Conditional statistics information was obtained for each type of turbulent structure detected, regarding the fluctuating velocity components (u',v' and w'), fluctuating vorticity components (ω'_x, ω'_y and ω'_z), Reynolds shear stress ($-u'v'$) and dissipation rate (ϵ). These quantities were averaged within the detected connected regions in the binary field. As already mentioned, it is important to emphasize that, despite the fact that the analysis was performed based on wall-normal-spanwise planes instead of 3D fields, differently from the standard PIV, tomo-PIV allows assessing all components of velocity and vorticity vectors, the 3D Q-criterion and dissipation quantities. The conditional statistics were computed from structures occupying approximately the same wall-normal position, averaging flow quantities spatially in wall-parallel slabs of ± 18 wall units and in time. So, turbulent structures that had their centres around the same distance from the wall were grouped to provide probability density functions, averages and root-mean-squares of flow quantities.

7.1 Mean fluctuating velocity components

Conditional mean values of fluctuating velocity components were computed for different wall-normal positions, in order to yield information on how the turbulent structures travel in relation to the mean flow. Results for mean fluctuating streamwise, wall-normal and spanwise velocity components are displayed, respectively in figures 9(a-c). In each figure, the data corresponding to the different structures detected, namely low- and high-speed regions, ejections, sweeps and vortices, are cued to the symbols described in the legend. The subscript CS refers to the statistics calculated with respect to these coherent structures. In the figure, the fluctuating velocity components are made dimensionless by the friction velocity u_τ. It should be mentioned that the mean values of the fluctuating velocity components displayed in figure 9 were determined in relation to the average of the entire flow, at a particular wall-normal position. So, values different from zero are possible within the areas occupied by the detected structures.

An observation of the mean fluctuating velocity components associated with the detected low-speed regions shown in figure 9(a) reveals negative streamwise values, indicating that these structures travel at speeds that are lower than the mean flow. These negative values were expected due to the definition assigned to these structures based on the streamwise velocity detection criteria described in Table 2. The low value observed for the position closest to the wall in the mean fluctuating streamwise velocity component can be attributed to to the expected increase in the population of low-speed streaks as the wall is approached (Kline et al., 1967, Robinson, 1991).

The small positive values observed in figure 9(b) for the mean wall-normal fluctuating velocity component reflect the upward movement of the low-speed regions. These positive values can be considered representative since they are larger than the estimated prevailing levels of experimental uncertainty. The negligible values for the mean spanwise fluctuating velocity component displayed in figure 9(c) indicate that the low-speed regions are, in average, aligned with the mean flow.

The results for the mean fluctuating velocity components associated with the detected high-speed regions shown also in figures 9(a-c) are nearly mirror images of the results just presented for the low-speed regions. The results indicate that the high-speed regions travel faster than the mean flow, moving

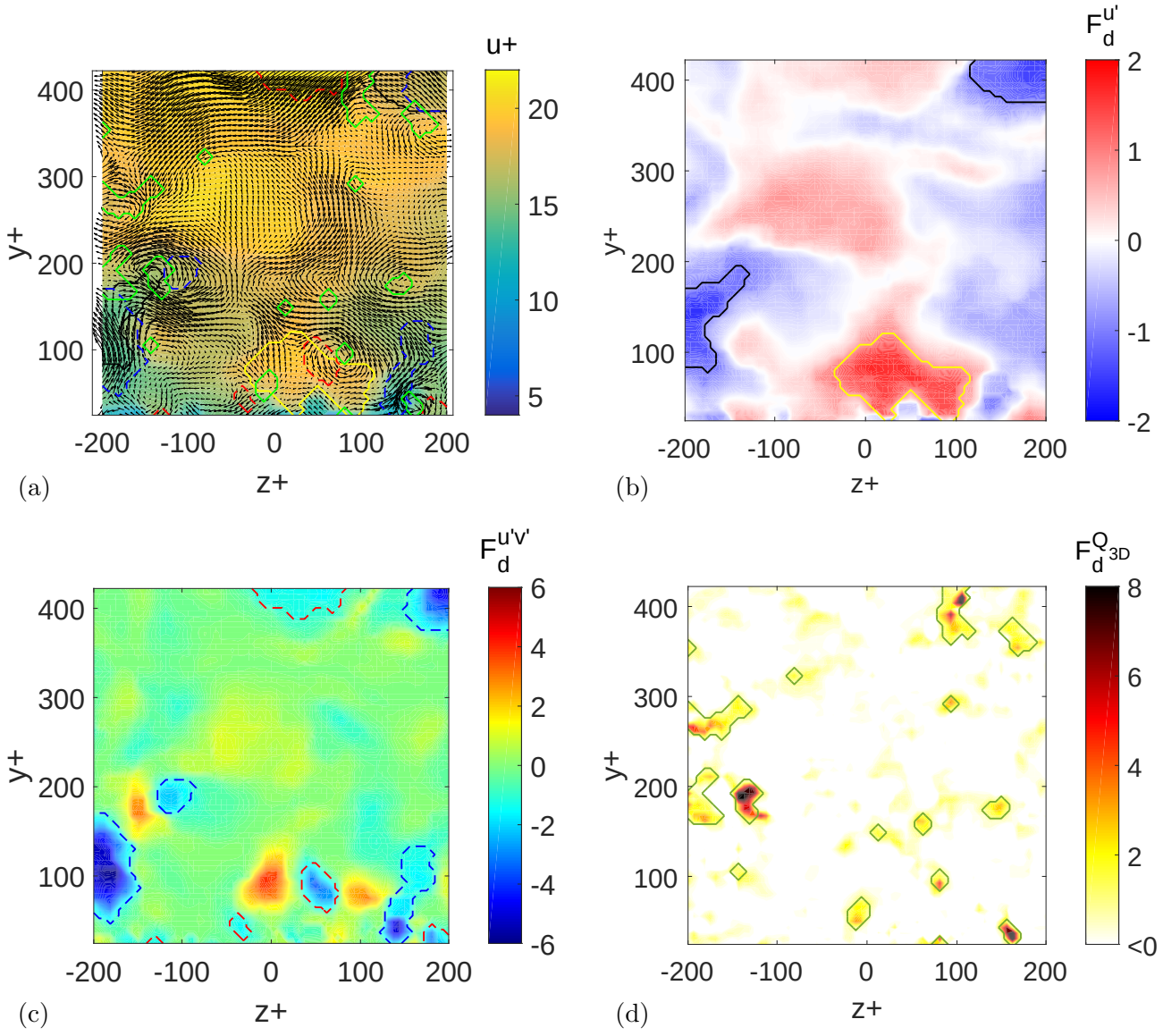

Figure 8: (a) Sample of instantaneous velocity field coloured by the magnitude of the streamwise velocity component. The superimposed contours refer to the detected structures: low-speed regions (—), high-speed regions (—), ejections (– –), sweeps (– –) and vortices (—). (b) Normalized field of detection function based on the fluctuating streamwise velocity showing contours of detected low- and high-speed regions. (c) Normalized field of detection function based on the Reynolds shear stress showing contours of detected ejections and sweeps. (d) Normalized field of the detection function based on the Q-criterion showing contours of detected vortices.

downward and aligned with the mean flow direction.

Attention is now turned to the conditional statistics results for the mean fluctuating components of the velocity associated with sweep and ejection regions displayed in figure 9. As can be verified in the figure, the profiles of mean streamwise velocity lie close for low-speed regions and ejections, and for high-speed regions and sweeps. This is and indication of the strong correlation between low-speed regions and ejections, and high-speed regions and sweeps. The positive values of the mean wall-normal component in figure 9(b) are larger for the ejections, as compared with those associated with the low-speed regions. Similarly, for the sweep regions, larger magnitudes of the negative mean wall-normal velocity component prevail, as compared to those of the high speed-regions. This means that ejection regions move slower than the mean streamwise flow ascending in the boundary layer at a faster rate than low-speed regions and the mean flow. Sweep regions, on the contrary, approach the wall at a larger velocity than the high speed regions, moving slower than the mean flow that surrounds them. The results of figure 9(b) also show that the ejections move upward at a faster rate than sweeps move downward. The negligible values for the mean spanwise velocity component observed in figure 9(c) for both the sweep and ejection regions, indicate that these structures are preferentially aligned with the mean flow, reinforcing its correlation with the low and high speed regions.

Lin (2006) investigated conditional statistics of turbulent structures employing stereo PIV in streamwise-spanwise planes located in the buffer layer at $10 < y^+ < 50$, for $Re_\theta = 7800$, in the same wind tunnel used in the present work. The results of that author showed similar conclusions with respect to the arrangement of the coherent structures as those just inferred from the conditional statistics of the mean fluctuating velocity components. This is an indication that relatively the same patterns of structures detected in the inner-region prevail in the log-region, with larger scales and less intensities, as will be reinforced along the text with the presentation of other conditional statistics.

The conditional statistics results for the mean fluctuating components of the velocity associated with the vortical structures are also displayed in figure 9. The results presented for the mean fluctuating velocities of the wall-normal and spanwise components show negligible values, and a slightly negative value for the streamwise mean component. These results should be analysed taking into consideration the prevailing levels of experimental uncertainties mentioned previously. It is seen that the small negative values found for the mean streamwise velocity are within the uncertainty levels and, for that reason, should be considered to be also negligible as those of other velocity components.

Carlier and Stanislas (2005) and Herpin et al. (2013) also found the streamwise velocity of vortical structures slightly under the flow velocity. They concluded that the differences detected were negligible. Elsinga et al. (2012) observed that, in average, the vortex elements were passively convected with the flow, despite not strictly following the instantaneous local flow velocity, in the outer region experiment of a turbulent boundary layer at $Re_\theta = 2460$ measured by a time-resolved tomo-PIV system. Lozano-Durán and Jiménez (2014) tracked coherent structures in DNSs of channel flows with Re_τ from 930 to 4200, in other to characterize these structures from birth to death. They also obtained the mean convection velocity of vortices equal to the local flow. In view of the results presented in figure 9, the vortical structures are, in average, seen to be convected with approximately the local flow velocity, which is in agreement with the results available in the literature (e.g., Adrian et al., 2000, Christensen and Adrian, 2001, Wu and Christensen, 2006, Herpin et al., 2010). Contrarily, Gao et al. (2011) obtained vortical eddies typically travelling at velocities of about 96% to 98% of that of the local mean flow from the analyses of direct numeric simulations of channel flows and a dual-plane stereo PIV experiment in a zero-pressure-gradient turbulent boundary layer. These velocities seem to be influenced by the type of vortices detected by these authors after their filtering procedures.

The present results seems to indicate that groups of vortical structures travel together with similar velocity, in agreement with the hairpin package model of Adrian et al. (2000). Some groups can be faster and others slower than the surrounding fluid, but, in average, they move with the same flow velocity. These finds can as well be interpreted as a disorganized movement of vortical structures that form vortex clusters, which, in average, are convected with flow velocity, in agreement with del Álamo et al. (2006).

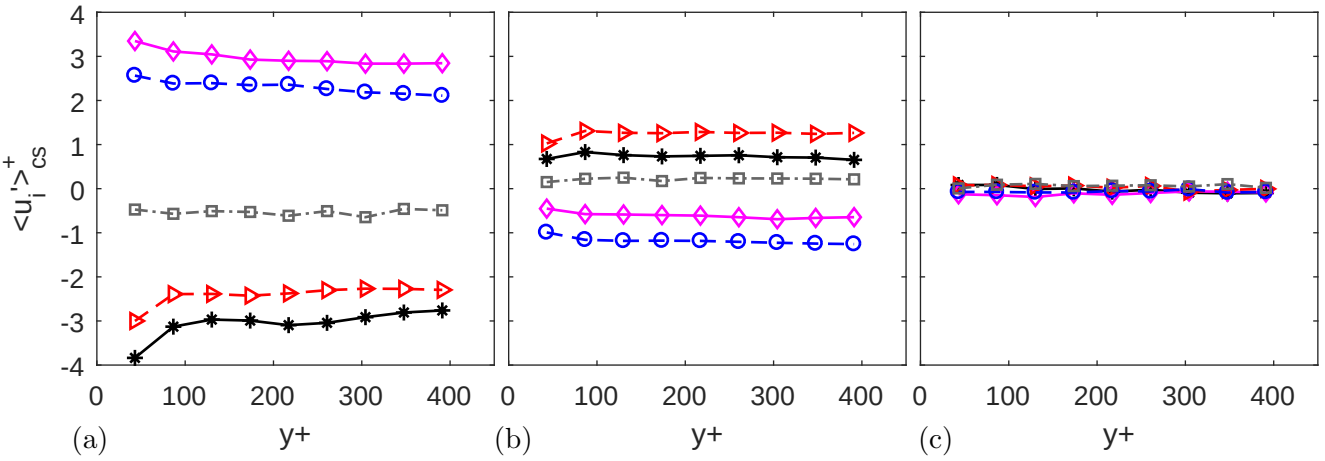

Figure 9: Mean fluctuating velocity components associated with the detected flow structures, as a function of the wall-normal coordinate: (a) mean streamwise velocity, (b) mean wall-normal velocity and (c) mean spanwise velocity. Legend: low-speed regions (–∗–), high-speed regions (–◇–), ejections (–▷–), sweeps (–○–) and vortices (–⊡–).

7.2 Root-mean-square of fluctuating velocity components

Figure 10 shows results for the root-mean-square of fluctuating velocity components associated with flow structures detected (superscript CS). These results are presented as a ratio to the root mean square values of correspondent velocity components determined for the overall flow (shown in figure 3(b)), at the same wall-normal positions. Figures 10(a-c) present the ratio of the RMS values, respectively for the streamwise, wall-normal and spanwise fluctuating components. In each figure, results are presented for low- and high-speed regions, ejections, sweeps and vortices, as indicated in the legend. It is important to mention that these root-mean-square values were computed based on the amount of structures around a particular wall-normal position. The computation did not take into account the area of the detected structures.

The results of Figure 10(a) show that the RMS values of the streamwise fluctuating velocity component associated with low- and high-speed regions, ejections and sweeps, are all above the value for the overall flow. These results demonstrate that these structures are responsible to transport an important amount of energy across the boundary layer flow in the log region. The RMS values for the wall-normal velocity components shown in figure 10(b) are slightly above those of the entire flow only for ejections and sweeps. For the other studied structures, the values are approximately of the same magnitude as those of the overall flow. The RMS of spanwise fluctuating velocity components presented in figure 10(c) are indistinguishable from the values of the complete flow. For vortical structures, the results of figures 10(a-c) present similar values for the RMS of the three velocity components and those of the overall flow. These findings are in line with Wu and Christensen (2006), which analysed the dispersion of streamwise velocity of vortices detected in the streamwise-wall-normal PIV plane for a channel flow with $Re_\tau = 1760$ and a boundary layer with $Re_\tau = 2350$, and also with Herpin et al. (2013), which studied the dispersion of streamwise velocity of vortices detected in the wall-normal-spanwise plane of a flat plate boundary layer at various Re_θ, ranging from 7630 to 18950.

The meandering and branching behaviour of low-speed regions close to the wall, reported extensively in the literature (e.g., Schoppa and Hussain, 2002, Hutchins and Marusic, 2007, Dennis and Nickels, 2011a) and observed in the instantaneous tomo-PIV visualizations of the present boundary layer flow (Martins et al., 2015a), are not revealed in these conditional statistics. The low-frequency, low-amplitude meandering nature of low-speed regions gives a very small contribution to the fluctuating streamwise and spanwise velocity components, as compared to the overall flow. That contributions can not be noticed in figure 10(a) and (c), since small variations near the wall in the RMS statistics of low- and also high-speed regions are within the computed uncertainty levels. The average statistics of fluctuating velocity,

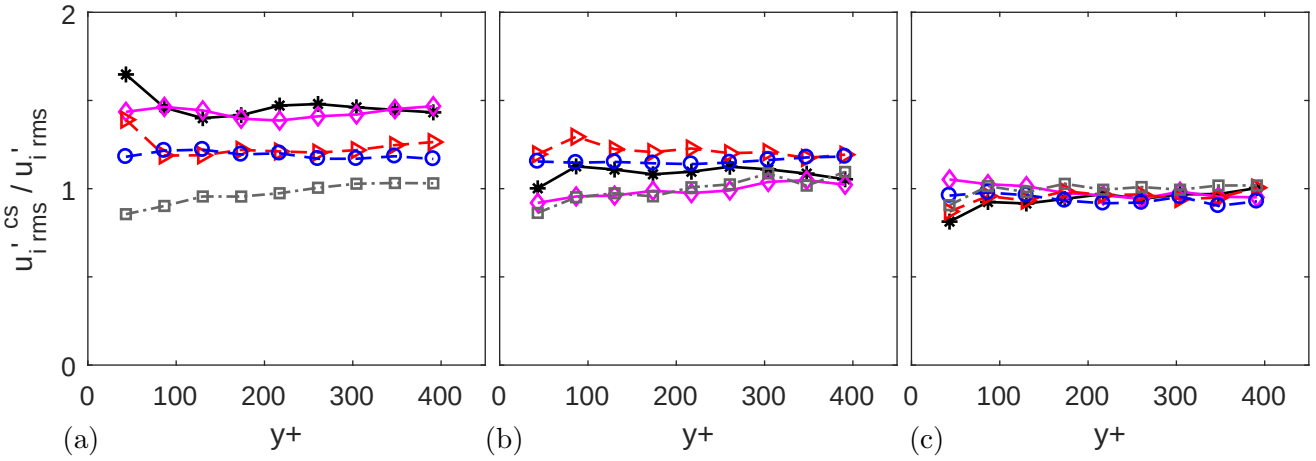

Figure 10: Root-mean-square of fluctuating velocity components associated with detected flow structures, as a function of wall-normal coordinate: (a) mean streamwise velocity, (b) mean wall-normal velocity and (c) mean spanwise velocity. Legend: low-speed regions (–∗–), high-speed regions (–◇–), ejections (–▷–), sweeps (–○–) and vortices (–⊡–).

presented in figure 9, equally hide the described meandering behaviour.

The information extracted from the velocity fields allows the assessment of the contribution of the flow structures to the root-mean-square of fluctuating streamwise velocity of the total field. For the low-speed regions, this contribution was of the order of 20% on average, associated to a structure area of about 13% of the total flow area. The contribution of high-speed regions was about 18%, associated with an area of about 12% of the total flow area. Similar contributions to the total root-mean-square of fluctuating streamwise velocity of large-scale low- and high-speed structures were reported by Dekou et al. (2016). In that work, the large-scale turbulent structures were analysed in the outer region of a flat-plate boundary layer by Linear Stochastic Estimation, employed to correlate velocity fields obtained in spanwise-wall-normal stereo-PIV planes and hot wire anemometry data, for Re_θ around 9800, utilizing the same wind tunnel as that of the present work.

The contribution of ejection structures to the total root-mean-square of fluctuating streamwise velocity was 19% on average, with a relative structure area of about 16% of the total flow area. Sweeps presented similar numbers. It should be mentioned that, as expected, large portions of the areas of ejections intercepted the low-speed regions, the same occurring in relation to sweeps and high-speed regions. RMS of wall-normal velocity fluctuations inside ejections and sweeps, were slightly above the global flow statistics. Ejection events contributed with 19% and sweep events with 18% to the total root-mean-square of this velocity component. The RMS of spanwise velocity profiles associated with turbulent structures and those of the surrounding flow were coincident, taking into account the uncertainty levels of the present tomo-PIV data.

The contributions of vortical structures regarding the root-mean-square of fluctuating velocity components to those of the entire flow were found to be negligible. The relative contribution of the fluctuation from each velocity component within the vortices were lower than 2%, with a relative structure area of about 2% of the total flow area.

7.3 Mean Reynolds shear stress

Conditional statistics for the Reynolds shear stress component, $-u'v'_{\mathrm{cs}}$, were calculated for the detected turbulent structures. The results are presented in figure 11, where the mean Reynolds shear stress component is plotted as a function of the wall-normal position, and divided by the corresponding mean values of the flow Reynolds shear stress measured at the same wall-normal position (displayed in figure 4(a)).

The results obtained show values for the Reynold shear stress associated with the ejection and sweep

regions that are from 2.5 to 3.5 larger than the values for the flow Reynolds shear stress at the same corresponding wall-normal positions. It is seen that the ejection regions present larger values than the sweep regions along the log layer investigated in the present study, which is in agreement with Wallace (2016). The contribution, in average, of the ejection and sweep regions to the total Reynolds shear stress were, respectively, 47% and 40%. These are significant numbers, especially if confronted with the areas occupied by these regions in the total flow, which were computed to be only 16% and 15%, respectively. The observation of higher contribution of ejections in relation to sweeps is in agreement with Lu and Willmarth (1973) and Lin (2006), although these authors computed even higher values than the ones reported here. Lu and Willmarth computed a conditional Reynolds shear stress at the near-wall region of a turbulent boundary layer at Re_θ of 4230 and 38000. They measured the Reynolds stress employing an X-wire probe and the quadrant event was triggered by another probe located at the at the edge of the viscous sublayer, which is a completely different feature detection of coherent structures from that used in the present work. It is remarkable that equivalent results were obtained by totally distinct measuring techniques.

Low- and high-speed regions also present significant contributions to the flow Reynolds shear stress, although not as pronounced as those from ejection and sweep regions. Low-speed regions contribute comparatively more than high-speed regions at positions closer to the wall, gradually matching the contributions associated with the high-speed regions at the end of the log layer. The higher contribution from low-speed regions was reported by many researchers (e.g., Talmon et al., 1986, Kang et al., 2007, Dennis and Nickels, 2011b, Dekou et al., 2016). The contribution from the low-speed regions to the total Reynolds shear stress was 36%, in average, while that from the high-speed regions represented 24%. These relative values of Reynolds shear stress contributions are similar to the values found by Dekou et al. (2016) of 40% and 25% for large-scale low- and high-momentum regions in the outer layer region.

Low- and high-speed regions were previously shown to be correlated with ejections and sweep regions according to figure 9. The conditional statistics results just presented for the Reynolds shear stress indicate that low- and high-speed regions and specially ejection and sweep events are responsible for most of the turbulence production in the log layer.

The conditional statistics associated with vortex regions of figure 11 present nearly identical values for Reynolds shear stress as those for the main flow, leading to the conclusion that vortices are not directly linked to the turbulent production along the log region, although they can induce other events related to production, such as ejection and sweeps (Robinson, 1991, Lin, 2006).

The present work identified vortical structures spread all over the flow. Nevertheless, they were predominantly found close to low-speed regions and ejections. Therefore, they seem to be indirectly correlated with the process of turbulence production in the near-wall region. That is why it is not surprising that most of turbulent models based on coherent structures in the literature include vortices. These vortices could explain the maintenance of these low-speed packages and the transportations of energetic fluid to the upper zones of the flow trough ejection events. The sweep events seem to be a consequence of mass conservation due to the fluid movements during these ejections. These processes are in agreement with the literature (Robinson, 1991), but the conditional statistics of the present tomo-PIV work are insufficient to explain these mechanisms and additional investigation is necessary.

7.4 Mean dissipation rate

Figure 12 shows the conditional statistics for the mean dissipation rate associated with low- and high-speed regions, ejections, sweeps and vortices. The mean dissipation rate values within the coherent structures, $< \epsilon >_{cs}$, are normalized by the dissipation rate of the flow (presented in figure 4(b)), at the same wall normal positions.

A general observation of the results of figure 12 shows that low-speed regions and ejections offer extra contributions to the flow dissipation rate. Even higher relative values of dissipation rate associated to low-speed and ejection regions at positions closer to the wall are observed, and can be attributed to the higher presence of vortices within these near-wall regions. High-speed regions and sweeps presented lower mean dissipation rate than that of the entire flow, for most part of the log region. A similar behaviour

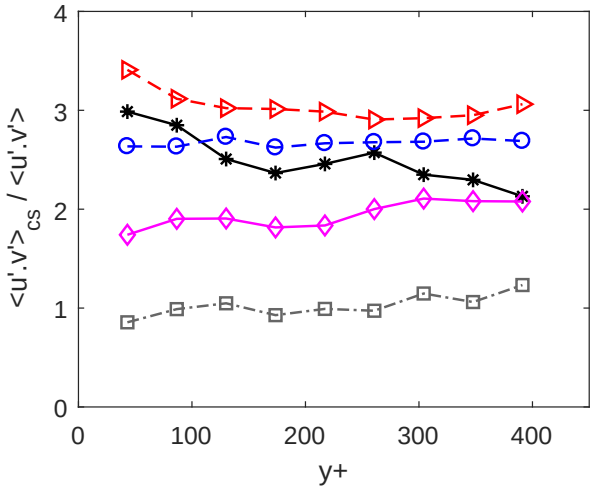

Figure 11: Mean Reynold shear stress in relation to the flow Reynolds shear stress, as a function of wall-normal distance associated to low-speed regions (–⋆–), high-speed regions (–◇–), ejections (–▷–), sweeps (–○–) and vortices (–⊡–).

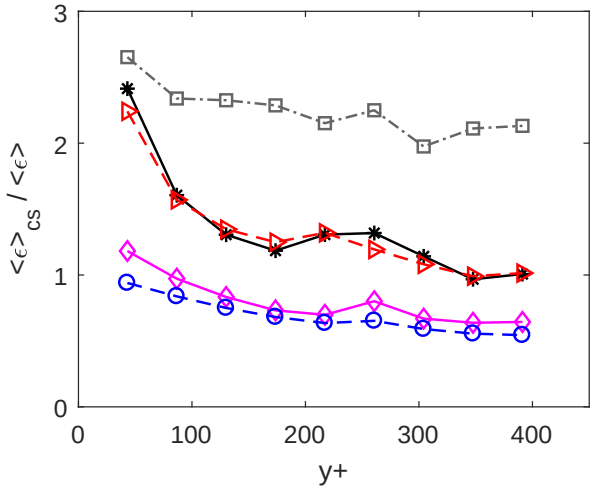

Figure 12: Mean dissipation rate in relation to the flow dissipation rate, as a function of wall-normal distance associated to low-speed regions (–⋆–), high-speed regions (–◇–), ejections (–▷–), sweeps (–○–) and vortices (–⊡–).

of the mean dissipation rate was also found by Kang et al. (2007). In that direct numerical simulation study of a channel flow with Re_τ of 800, the increase in the dissipation rate was attributed to the higher probability of existence of vortices inside low-momentum regions than inside high-momentum regions. These findings were in agreement with Dennis and Nickels (2011b), which observed the vast majority of vortices nearby the low-speed regions in their high-speed stereo PIV measurements of the near-wall region of a zero pressure-gradient boundary layer with moderate Reynolds number. Similar results also were obtained by Elsinga et al. (2010) employing the tomo-PIV technique to measure the near-wall region of a supersonic turbulent boundary layer.

The relative contribution of low-speed regions and ejections to the total dissipation rate was, on average, 21% and 24%, respectively, in the present work. In contrast, the mean dissipation rate associated with high-speed regions and sweeps were around 10%, with relative areas of 12% and 15%, respectively.

Conditional statistics within the detected vortex structures present values of the dissipation rate that are between 2 to 3-fold more intense than the values for the entire flow, at the corresponding wall-normal positions. The contribution from vortex structures to the total dissipation rate was, in average, 5%, occupying a relative structure area of only 2% of the total flow area.

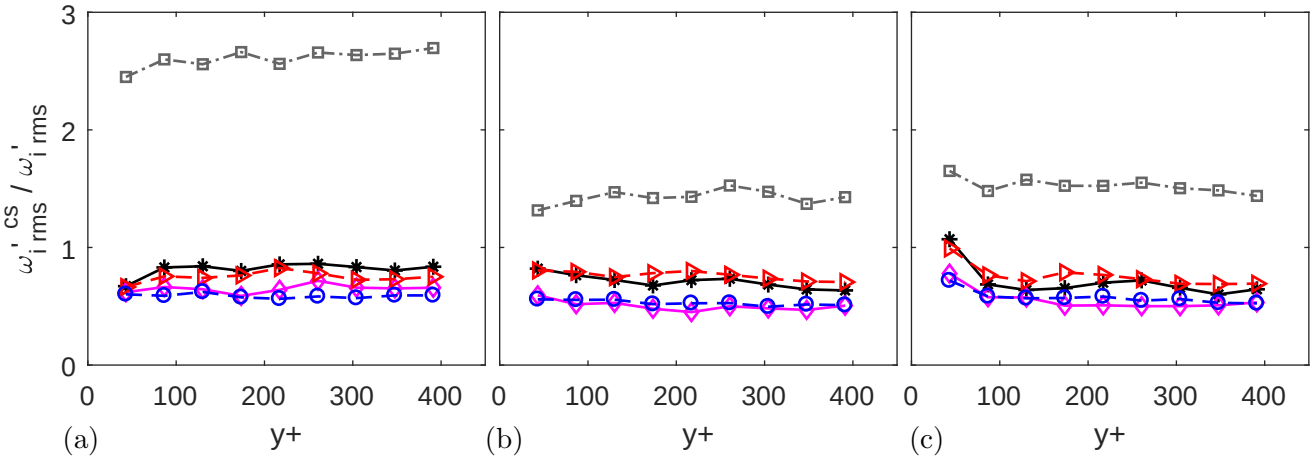

Figure 13: Root-mean-square of fluctuating vorticity components associated with detected flow structures, as a function of wall-normal coordinate: (a) streamwise, (b) wall-normal and (c) spanwise vorticities. Legend: low-speed regions (–⋆–), high-speed regions (–◇–), ejections (–▷–), sweeps (–○–) and vortices (–□–).

Although conditional statistics of mean dissipation rate alone can not provide detailed information about the self-sustaining turbulence process, in which the energy from the main flow is subsequently transported and finally dissipated by viscosity in the small scales (Jiménez, 2013, Lozano-Durán and Jiménez, 2014), results obtained in the present work indicate that the energy transported and produced by low- and high-speed regions, ejection and sweeps seems to be transferred among these structures and dissipated by the vortices.

7.5 Root-mean-square of fluctuating vorticity

The conditional statistics for the root-mean-square of fluctuating vorticity components for all the identified structures are presented in figure 13. For comparison purposes, each component of the RMS vorticity within the coherent structure (superscript CS) is presented divided by the RMS vorticity of the entire flow (presented in figure 5), calculated at the corresponding wall-normal position.

In general, the results for low-speed, high-speed, ejections and sweep regions present a decrease in all RMS components of the vorticity, as compared to the flow vorticiy components. A more detailed look at the figures, however, reveals a stronger drop in the RMS value for all fluctuating component of vorticity associated with high-speed regions and sweeps in relation to the values prevailing in the entire flow. These more detailed observations, however should be interpreted with caution, since the levels of experimental uncertainty are not too distinct from the differences observed.

A totally different picture emerges from the analysis of the results for the RMS fluctuating vorticity components associated with the vortical areas detected by the Q-criterion employed. The results display a significant increase in the RMS values of all vorticity components in relation to the values for the flow. Further, it can be observed that the increase in the streamwise component of the fluctuating vorticity is above that of the other components. Indeed, the streamwise vorticity component associated with the vortical areas contributed to 5%, in average, to the total root-mean-square of streamwise fluctuating vorticity of the flow, while wall-normal vortex fluctuating vorticity and spanwise vortex fluctuating vorticity were responsible, each one, for about 3% of the total, with an relative area of only 2%, as mentioned before. This difference seems to be the result of the presence of a larger number of *quasi*-streamwise vortices associated with the vortical regions in the log layer. Robinson (1991) also find high occurrence of *quasi*-streamwise and spanwise vortices in the logarithmic region, which was interpreted by Adrian et al. (2000) as being parts of a larger harpin vortex structure.

7.6 Vortex elevation angle

In addition to the above mentioned quantities, the inclination angle of any individual vortex structure intersecting the measurement plane can be computed based on the orientation of the fluctuating vorticity vector at the vortex core. Elevation angle is proposed in order to analyse the vortex orientation and the sense of rotation, i.e., the direction of the fluctuating vorticity vector at the vortical axis. The elevation angle (θ_e), which defines the angle between the vorticity vector and the wall (streamwise-spanwise plane) with values between $-90°$ and $+90°$, is defined as (Ganapathisubramani et al., 2006)

$$\theta_e \;=\; \arctan\left(\frac{\omega'_y}{\sqrt{\omega'^2_x+\omega'^2_z}}\right) \quad . \tag{7}$$

The probability density function (PDF) of the vortex elevation angle for the present tomo-PIV measurements was computed using all vortices that belong to the logarithmic region, i.e., y^+ from 100 to 400 wall units, in order to better converge vortex conditional statistics, since no significant variation was observed in the distribution shapes computed at distinct wall-normal positions inside that region.

Figure 14 shows the probability density functions of the elevation angle of the present tomo-PIV data for vortices classified based on the previously presented detection function, $F_d^{Q_{3D}} \geq 1$, and for inclined vortices classified based on the joint detection function $F_d^{Q_{xz}} \geq 1$ and $F_d^{Q_{yz}} \geq 1$ at the region $100 < y^+ < 400$. The vortical detection functions $F_d^{Q_{xz}}$ and $F_d^{Q_{yz}}$ are 2D versions of $F_d^{Q_{3D}}$ where the Q-criterion is computed based only on the streamwise and spanwise components of the velocity vector, and on the wall-normal and spanwise velocity components, respectively. PDFs of the vortex elevation angle of Ganapathisubramani et al. (2006) data at $y^+ = 110$ employing two different detection functions are also plotted for comparison.

The distribution of the elevation angle for all population of vortical structures ($F_d^{Q_{3D}} \geq 1$) in figure 14 presents just one peak at zero and concentrates about 95% of the vortex inclinations between -40° and 40°, indicating that most of the analysed vortical structures are aligned with the streamwise direction. The vortex statistics just presented in the previous sections are most related to these *quasi*-streamwise vortices that populate the turbulent structures detected. The wide variety of inclinations of vortical structures, in addition to the variety of vortical shapes (Martins et al., 2015a), are in agreement with the vortex cluster model of del Álamo et al. (2006), in which complex worm-like vortices are present. This behaviour is also in line with Jiménez (2013), which reported that the vorticity tends to become more isotropic far from the wall, reflecting in a diversity of orientations and geometries of vortical structures.

In order to favour the detection of inclined vortices, a different detection function is proposed. The vortex detection now employed threshold levels equal to one in two normalized functions based on 2D Q-criteria, one computed within the streamwise-spanwise plane ($F_d^{Q_{xz}}$) and other computed within the wall-normal-spanwise plane ($F_d^{Q_{yz}}$). Figure 14 shows the change in the PDF distribution employing the detection function for inclined vortices. This detection function is able to remove the influence of *quasi*-streamwise vortices. The PDF shows two peaks around $-40°$ and 40°, that where previously hidden in the PDF of all vortical structures ($F_d^{Q_{3D}} \geq 1$). The peaks found are in close agreement with Dennis and Nickels (2011a), which obtained hairpin-like vortices with inclinations between 35° and 40° from the conditional statistics of reconstructed 3D velocity fields from stereo PIV measurements of a moderate Reynolds number turbulent boundary layer. The present results are also in line with the vortex inclinations from conditional average of Schröder et al. (2011). They found inclined vortical structures evolving in time from 45° to 35° in the logarithmic region of a turbulent boundary layer at $Re_\theta = 2460$ using time-resolved tomographic PIV. Sabatino and Rossmann (2016) observed as well a 34° inclination of legs of a regenerating hairpin vortex visualized by tomo-PIV in a laminar boundary layer. On the other hand, Jodai and Elsinga (2016) found slightly smaller hairpin-leg inclinations ranging from 8° to 12° with hairpin necks from 45° to 80° in a turbulent boundary layer of $Re_\tau = 2038$ employing time-resolved tomo-PIV.

The bimodal distribution in figure 14 is related to the homogeneity of almost equal number of clockwise (49%) and counter-clockwise (51%) vortices. It is important to mention that these vortical motions are not

always paired. A visual inspection of the instantaneous 3D reconstructed turbulent structure for the same tomo-PIV data (Martins et al., 2015a) revealed most of vortical structures with asymmetrical shapes. Of course some of apparently asymmetrical vortices observed might be part of a bigger symmetrical structure deteriorated as a result of spatial filtering due to the interrogation windows employed in the vector computation, time filtering due to the sampling frequency, and amount of noise in the instantaneous fields. The preferred asymmetrical-shaped vortices can be explained as a consequence of their faster autogeneration as compared to symmetric hairpins (Robinson, 1991), which is more noticeable in high Reynolds number flows. The almost symmetrical distribution with two peaks is in agreement with the existence of cane vortices (Carlier and Stanislas, 2005, Schoppa and Hussain, 2002, Dennis and Nickels, 2011a, Herpin et al., 2013) and also with *quasi*-symmetrical hairpin vortices (Adrian et al., 2000, Christensen and Adrian, 2001), although the latter ones seem to have small frequency of occurrence (Robinson, 1991, Schoppa and Hussain, 2002, Sheng et al., 2008, del Álamo et al., 2006, Dennis and Nickels, 2011a, Jodai and Elsinga, 2016).

It is important to mention that, although from a kinematic point of view, the models of Adrian et al. (2000) and Del Álamo et al. (2004) are statistically comparable, these models are not similar with respect to the structure dynamics. As emphasized by Lozano-Durán and Jiménez (2014), the hairpin vortices are seen as the cause of the low-speed and ejection regions, while the clusters of vortices of Del Álamo et al. (2004) are considered as a consequence of the former structures.

The vortex elevation angle of Ganapathisubramani et al. (2006) data at $y^+ = 110$ is also presented in figure 14. Ganapathisubramani et al. (2006) performed a dual-streamwise-spanwise-plane PIV to compute the full velocity gradient tensor in the near-wall region of a wind-tunnel turbulent boundary layer at $Re_\theta = 2800$, three times lower than the present experimental Reynolds number. Ganapathisubramani et al. (2006) studied the vortex orientation based on the vorticity vector and employed similar procedure of the present work to extract vortices. The differences between the present work and their study were mainly in the use of the 3D swirling strength criterion ($\lambda_{ci\,3D}$) as a detection function (Chakraborty et al., 2005), a growing algorithm to segment vortices and the orientation of the investigation plane. In figure 14, the probability density function of elevation angles computed before and after filtering vortices with a in-plane orientation are presented. Ganapathisubramani et al. (2006) employed the 2D swirling strength criterion ($\lambda_{ci\,xz} > 0$), which should behave equivalently to the Q-criterion (Chakraborty et al., 2005, Martins et al., 2016), in order to remove vortices aligned with the measuring plane. The filtered PDF shows a distribution with two peaks, one at $-45°$ and other at $45°$, which were obscured in the distribution before filtering. The peaks were ascribed to the legs of hairpin-like vortices with negative and positive fluctuating streamwise vorticity, respectively, according to these authors. These findings were later confirmed by the study of Gao et al. (2011). These peak values are in agreement with the present work. Slight differences seem to be related to the bin resolution of the present data, since the amount of vortical structures detected do not allow converged statistics with better resolution of θ_e.

As can be also observed in figure 14, the PDF of the elevation angle for all population of vortical structures ($F_d^{Q_{3D}} \geq 1$) from the present tomo-PIV measurements detects more vortices aligned with respect to the main flow than the correspondent unfiltered PDF ($\lambda_{ci\,3D}$) of Ganapathisubramani et al. (2006), which presents a wider distribution. This fact seems to be a consequence mainly to the orientation of the investigation plane, since the wall-normal-spanwise plane is more sensitive to detect vortices with lower values of θ_e.

8 Conclusion

The present tomo-PIV measurements were obtained in a flat-plate turbulent boundary layer flow with a momentum-thickness Reynolds number of 8500 at $25 < y^+ < 450$. The six-camera experiment provided quantitative information related to 3D velocity components, 3D vorticity components, Reynolds shear stress and dissipation fields in a wall-normal-spanwise volume at the log-region. The uncertainty associated with the measurements were accessed, showing the good quality of the data.

Statistical flow characteristics of the boundary layer from over 1200 vector fields were presented.

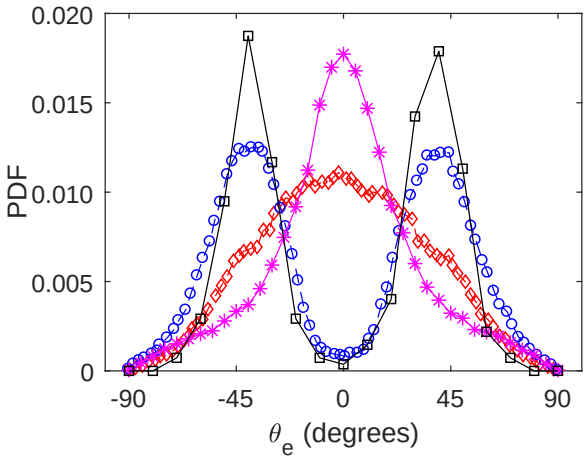

Figure 14: Probability density functions of elevation angle of vortices at $100 < y^+ < 400$ from tomo-PIV data detected employing $F_d^{Q_{3D}} \geq 1$ (–✳–) and employing $F_d^{Q_{xz}} \geq 1$ together with $F_d^{Q_{yz}} \geq 1$ (–□–). For comparison, it was plotted the probability density functions of elevation angle of vortices detected on the streamwise-spanwise PIV plane at $y^+ = 110$ of Ganapathisubramani et al. (2006) employing detection function based on the $\lambda_{ci\,3D}$ (–◇–) and additionally using $\lambda_{ci\,xz} > 0$ (–○–).

Good agreement among tomographic PIV, hot-wire anemometer data and direct numerical simulations from the literature was observed in terms of velocity profiles, turbulent fluctuations, probability density functions, vorticity, Reynolds shear stress and dissipation rate.

Turbulent structures, namely, low- and high-speed regions, ejections, sweeps and vortices, were detected by means of conditional sampling. Analyses of the conditional statistics within these structures delivered quantitative information of the relative contribution of each type of coherent structure to the overall turbulent flow.

The low- and high-speed conditional statistics revealed that, in average, the low-speed regions moved upwards while the high-speed regions moved towards the wall. During the movement, these structures are able to transport a significant amount of energy, identified as higher values of the root-mean-square of the fluctuating streamwise component and Reynolds shear stress associated with these structures, as compared to those of the neighbouring flow. These findings were in agreement with the literature and indicate the strong influence of ejection and sweep events in the flow.

The ejection and sweep events displayed higher values for the root-mean-square of the fluctuating streamwise and wall-normal components than those of the neighbouring flow. The Reynolds shear stress values calculated within ejection structures were remarkably higher than those within the sweep structures, both values being higher than the values computed for the complete flow statistics, which is in agreement with studies from other researchers. These findings lead to the conclusion that, among the turbulent structures studied in the present work, ejection and sweep structures are the major contributors to turbulent production.

Vortical structures were found to be, in average, convected with the local flow velocity. No difference was found between the statistics computed at vortex structures and the statistics of the global flow regarding the turbulent fluctuations and Reynolds shear stress, leading to the conclusion that the vortices are not directly linked to the turbulent production, although they can induce other events that are related to production, as ejections and sweeps. Contrarily, vortex conditional statistics presented dissipation values remarkably above those from the complete flow statistics as expected, since these structures are the main responsible for the turbulent energy dissipation in the near-wall region of the boundary-layer flow. Higher dissipation rates were observed close to the wall, where most high intensity vortices were detected. Results support the model for the self-sustaining turbulence process, in which the energy transported and produced by low- and high-speed regions, ejection and sweeps are transferred to other structures, in which merging and splitting mechanisms can be present, and then dissipated by vortices under the influence of viscosity. Details of the mechanisms of this multi-scale process can not be directly

extracted from the present conditional statistics analyses. The picture can be more complicated than a direct cascade from large to small coherent structures, as point out by Lozano-Durán and Jiménez (2014).

The present work identified vortical structures spread all over the flow. Nevertheless, they were predominantly found close to low-speed regions and ejections. From the present analyses, no single vortex pattern seems representative of the wide variety of shapes and inclinations, although asymmetric vortical structures were the most frequent displaying a considerable amount of *quasi*-streamwise vortices and inclined vortices at a characteristic elevation angle of about $\pm 40°$. The vortices showed similar frequency of occurrence of clockwise and counter-clockwise rotation. The preferred asymmetrical-shaped vortices seem to be a consequence of their faster autogeneration as compared to symmetric hairpins, which is more noticeable in high Reynolds number flows.

The conditional statistics on the coherent structures at the log region of the present work were in good agreement with the statistics for structures found at the inner region (Lin, 2006) and also at the outer region of the boundary layer (Dekou et al., 2016), which suggest some possibility of a general structure organization. Despite the fact that the structures shape and arrangement presented near the wall seem to differ from the large scale motions at the outer region, mainly due to the shear and viscous effects in the former region, the similar conditional statistics point to a general structure organization at different stage of evolution. This idea is in line to some works from literature (e.g., Adrian et al., 2000, del Álamo et al., 2006, Stanislas, 2017), although it is far from being a consensus. Further experimental and numerical studies should be pursued in order to draw a picture of this general structure and to confirm this hypothesis.

Acknowledgements

This work was carried out within the framework of the joint supervision of the doctoral program of Fabio Martins held at PUC-Rio (Brazil) and Centrale Lille (France). It was funded by the Mechanical Engineering Department of PUC-Rio and the Brazilian scholarship CAPES number BEX 9249/12-5. The experiment was performed at LML with a financial support of AFDAR European project, ANR Vive3D contract and CISIT. The authors acknowledge L. David, L. Thomas, B. Tremblais and P. Braud, from Pprime, B. Lecordier, G. Godard and C. Gobin, from Coria, S. Coudert and A. C. Avelar, from LML.

References

Atkinson, C., Buchmann, N., Amili, O., and Soria, J. (2014). On the appropriate filtering of piv measurements of turbulent shear flows. *Experiments in Fluids*, 55(1):1–15.

Atkinson, C., Coudert, S., Foucaut, J.-M., Stanislas, M., and Soria, J. (2011). The accuracy of tomographic particle image velocimetry for measurements of a turbulent boundary layer. *Experiments in fluids*, 50(4):1031–1056.

Balakumar, B. and Adrian, R. (2007). Large-and very-large-scale motions in channel and boundary-layer flows. *Philosophical Transactions of the Royal Society of London A: Mathematical, Physical and Engineering Sciences*, 365(1852):665–681.

BIPM, IEC, IFCC, ILAC, ISO, IUPAC, IUPAP, and OIML (2008). *Evaluation of Measurement Data – Guide to the Expression of Uncertainty in Measurement.* JCGM 100:2008.

Carlier, J. and Stanislas, M. (2005). Experimental study of eddy structures in a turbulent boundary layer using particle image velocimetry. *Journal of Fluid Mechanics*, 535(36):143–188.

Chakraborty, P., Balachandar, S., and Adrian, R. (2005). On the relationships between local vortex identification schemes. *Journal of Fluid Mechanics*, 535(2005):189–214.

Christensen, K. and Adrian, R. (2001). Statistical evidence of hairpin vortex packets in wall turbulence. *Journal of Fluid Mechanics*, 431:433–443.

Corino, E. and Brodkey, R. (1969). A visual investigation of the wall region in turbulent flow. *Journal of Fluid Mechanics*, 37(01):1–30.

Dekou, R., Foucaut, J.-M., Roux, S., and Stanislas, M. (2016). Large-scale organization of a near-wall turbulent boundary layer. In *Progress in Wall Turbulence 2*, pages 335–346. Springer.

Del Álamo, J., Jiménez, J., Zandonade, P., and Moser, R. (2004). Scaling of the energy spectra of turbulent channels. *Journal of Fluid Mechanics*, 500:135–144.

del Álamo, J., Jiménez, J., Zandonade, P., and Moser, R. (2006). Self-similar vortex clusters in the turbulent logarithmic region. *Journal of Fluid Mechanics*, 561:329–358.

Dennis, D. and Nickels, T. (2011a). Experimental measurement of large-scale three-dimensional structures in a turbulent boundary layer. part 1. vortex packets. *Journal of Fluid Mechanics*, 673:180–217.

Dennis, D. and Nickels, T. (2011b). Experimental measurement of large-scale three-dimensional structures in a turbulent boundary layer. part 2. long structures. *Journal of Fluid Mechanics*, 673:218–244.

Elsinga, G., Adrian, R., Van Oudheusden, B., and Scarano, F. (2010). Three-dimensional vortex organization in a high-reynolds-number supersonic turbulent boundary layer. *Journal of Fluid Mechanics*, 644:35–60.

Elsinga, G., Poelma, C., Schröder, A., Geisler, R., Scarano, F., and Westerweel, J. (2012). Tracking of vortices in a turbulent boundary layer. *Journal of Fluid Mechanics*, 697:273–295.

Elsinga, G., Scarano, F., Wieneke, B., and van Oudheusden, B. (2006). Tomographic particle image velocimetry. *Experiments in Fluids*, 41(6):933–947.

Foucaut, J.-M., Carlier, J., and Stanislas, M. (2004). Piv optimization for the study of turbulent flow using spectral analysis. *Measurement Science and Technology*, 15(6):1046.

Foucaut, J.-M., Coudert, S., Avelar, A., Lecordier, B., Godard, G., Gobin, C., Thomas, L., Braud, P., and David, L. (2011). Experiment of high repetition tomographic piv in a high reynolds number turbulent boundary layer wind tunnel. In *PIV'11 – Ninth International Symposium on Particle Image Velocimetry*.

Foucaut, J.-M., Cuvier, C., Stanislas, M., and George, W. K. (2016). Quantification of the full dissipation tensor from an l-shaped spiv experiment in the near wall region. In *Progress in Wall Turbulence 2*, pages 429–439. Springer.

Fuchs, T., Hain, R., and Kähler, C. (2016). Uncertainty quantification of three-dimensional velocimetry techniques for small measurement depths. *Experiments in Fluids*, 57(5):73.

Gao, Q., Ortiz-Duenas, C., and Longmire, E. (2011). Analysis of vortex populations in turbulent wall-bounded flows. *Journal of Fluid Mechanics*, 678:87–123.

Gonzalez, R. (2009). *Digital image processing*. Pearson Education India.

Head, M. and Bandyopadhyay, P. (1981). New aspects of turbulent boundary-layer structure. *Journal of Fluid Mechanics*, 107:297–338.

Herpin, S., Stanislas, M., Foucaut, J.-M., and Coudert, S. (2013). Influence of the reynolds number on the vortical structures in the logarithmic region of turbulent boundary layers. *Journal of Fluid Mechanics*, 716:5–50.

Herpin, S., Stanislas, M., and Soria, J. (2010). The organization of near-wall turbulence: a comparison between boundary layer spiv data and channel flow dns data. *Journal of Turbulence*, 11.

Hoyas, S. and Jiménez, J. (2008). Reynolds number effects on the reynolds-stress budgets in turbulent channels. *Physics of Fluids*, 20(10):101511.

Hunt, J., Wray, A., and Moin, P. (1988). Eddies, streams, and convergence zones in turbulent flows. In *Studying Turbulence Using Numerical Simulation Databases, 2*, volume 1, pages 193–208.

Hutchins, N. and Marusic, I. (2007). Evidence of very long meandering features in the logarithmic region of turbulent boundary layers. *Journal of Fluid Mechanics*, 579:1–28.

Jiménez, J. (2013). Near-wall turbulence. *Physics of Fluids*, 25(10):101302.

Jodai, Y. and Elsinga, G. (2016). Experimental observation of hairpin auto-generation events in a turbulent boundary layer. *Journal of Fluid Mechanics*, 795:611–633.

Kang, S.-J., Tanahashi, M., and Miyauchi, T. (2007). Dynamics of fine scale eddy clusters in turbulent channel flows. *Journal of Turbulence*, 8:N52.

Kline, S., Reynolds, W., Schraub, F., and Runstadler, P. (1967). The structure of turbulent boundary layers. *Journal of Fluid Mechanics*, 30(04):741–773.

Lin, J. (2006). *Étude détaillée des structures cohérentes de la zone tampon de la turbulence de paroi à l'aide de données de PIV stéréoscopique*. PhD thesis, École Centrale de Lille.

Lozano-Durán, A. and Jiménez, J. (2014). Time-resolved evolution of coherent structures in turbulent channels: characterization of eddies and cascades. *Journal of Fluid Mechanics*, 759:432–471.

Lu, S. and Willmarth, W. (1973). Measurements of the structure of the reynolds stress in a turbulent boundary layer. *Journal of Fluid Mechanics*, 60(03):481–511.

Martins, F., Foucaut, J.-M., Azevedo, L., and Stanislas, M. (2015a). Near-wall study of a turbulent boundary layer using high-speed tomo-piv. *Progress in Wall Turbulence 2: Understanding and Modelling*, 23:347–356.

Martins, F., Foucaut, J.-M., Thomas, L., Azevedo, L., and Stanislas, M. (2015b). Volume reconstruction optimization for tomo-piv algorithms applied to experimental data. *Measurement Science and Technology*, 26(8):085202.

Martins, R., Pereira, A., Mompean, G., Thais, L., and Thompson, R. (2016). An objective perspective for classic flow classification criteria. *Comptes Rendus Mécanique*, 344(1):52–59.

Adrian, R., Meinhart, C., and Tomkins, C. (2000). Vortex organization in the outer region of the turbulent boundary layer. *Journal of Fluid Mechanics*, 422:1–54.

Ganapathisubramani, B., Longmire, E., and Marusic, I. (2006). Experimental investigation of vortex properties in a turbulent boundary layer. *Physics of Fluids*, 18(5):055105.

Robinson, S. (1991). The kinematics of turbulent boundary layer structure. *NASA Technical Memorandum*, 91:26465.

Roerdink, J. and Meijster, A. (2000). The watershed transform: Definitions, algorithms and parallelization strategies. *Fundamenta Informaticae*, 41(1-2):187–228.

Sabatino, D. and Rossmann, T. (2016). Tomographic piv measurements of a regenerating hairpin vortex. *Experiments in Fluids*, 57(1):6.

Scarano, F. (2013). Tomographic piv: principles and practice. *Measurement Science and Technology*, 24(1):012001.

Schoppa, W. and Hussain, F. (2002). Coherent structure generation in near-wall turbulence. *Journal of fluid Mechanics*, 453(1):57–108.

Schröder, A., Geisler, R., Staack, K., Elsinga, G., Scarano, F., Wieneke, B., Henning, A., Poelma, C., and Westerweel, J. (2011). Eulerian and lagrangian views of a turbulent boundary layer flow using time-resolved tomographic piv. *Experiments in fluids*, 50(4):1071–1091.

Sciacchitano, A. and Wieneke, B. (2016). Piv uncertainty propagation. *Measurement Science and Technology*, 27(8):084006.

Sheng, J., Malkiel, E., and Katz, J. (2008). Using digital holographic microscopy for simultaneous measurements of 3d near wall velocity and wall shear stress in a turbulent boundary layer. *Experiments in fluids*, 45(6):1023–1035.

Smith, C. and Walker, J. (1997). Sustaining mechanisms of turbulent boundary layers: the role of vortex development and interactions. *Self-sustaining Mechanism of Wall Turbulence. Boston: Computational Mechanics Publications*, 47.

Stanislas, M. (2017). Near wall turbulence: An experimental view. *Physical Review Fluids*, 2(10):100506.

Stanislas, M., Perret, L., and Foucaut, J.-M. (2008). Vortical structures in the turbulent boundary layer: a possible route to a universal representation. *Journal of Fluid Mechanics*, 602:327–382.

Talmon, A., Kunen, J., and Ooms, G. (1986). Simultaneous flow visualization and reynolds-stress measurement in a turbulent boundary layer. *Journal of Fluid Mechanics*, 163:459–478.

Theodorsen, T. (1952). Mechanism of turbulence. In *2nd Midwestern Conference on Fluid Mechanics*, Ohio State University, Columbus, Ohio.

Thomas, L., Tremblais, B., and David, L. (2014). Optimisation of the volume reconstruction for classical tomo-piv algorithms (mart, bimart and smart): synthetic and experimental studies. *Measurement Science and Technology*, 25(3):035303.

Wallace, J. (2016). Quadrant analysis in turbulence research: history and evolution. *Annual Review of Fluid Mechanics*, 48:131–158.

Wallace, J., Eckelmann, H., and Brodkey, R. (1972). The wall region in turbulent shear flow. *Journal of Fluid Mechanics*, 54(01):39–48.

Wieneke, B. (2008). Volume self-calibration for 3d particle image velocimetry. *Experiments in Fluids*, 45(4):549–556.

Wu, Y. and Christensen, K. T. (2006). Population trends of spanwise vortices in wall turbulence. *Journal of Fluid Mechanics*, 568:55–76.

Zhou, J., Adrian, R., Balachandar, S., and Kendall, T. (1999). Mechanisms for generating coherent packets of hairpin vortices in channel flow. *Journal of Fluid Mechanics*, 387:353–396.